CHINA FOUNDRY Research & Development
Vol. 23 No. 2 March 2026
www.springer.com/41230
https://doi.org/10.1007/s41230-026-5062-0

Microstructure and tribological properties of Y_2O_3-doped Fe-based alloy coatings by laser cladding

Huo-ping Zhao[1], Li-yao Li[1], *Ming-xue Shen[1], Qiang Hu[2], Han-yu Zhou[1], Ye-long Xiao[1], De-ying Li[1], and Shao-peng Liu[1]

1. School of Materials Science and Engineering, East China Jiao Tong University, Nanchang 330013, China

2. Institute of Applied Physics, Jiangxi Academy of Sciences, Nanchang 330095, China

Abstract: The laser-clad Fe45 alloy coating inherently comprises multiple crystalline phases, resulting in a heterogeneous microstructural distribution that influences its performance. In this study, the rare earth yttria (Y_2O_3) was employed to modify laser-clad Fe45 alloy coatings, and the effects of Y_2O_3 addition on their microstructure, microhardness, and tribological properties were investigated. As the Y_2O_3 content increases from 0% to 0.3wt.%, the dominant microstructure transforms from columnar crystals to fine cellular and equiaxed crystals. The modified coating with 0.3wt.% Y_2O_3 achieves a surface hardness of 568 $HV_{0.3}$ and a wear volume of 1,735.41 μm^3, representing a 14.06% increase in hardness and a 51.16% reduction in wear volume compared to the undoped coating. Further increasing the Y_2O_3 content from 0.3wt.% to 0.9wt.% gradually leads to the emergence of a coarser feather-like microstructure, characterized by a dendritic framework with inter-dendritic equiaxed crystals. Concurrently, both the hardness and wear resistance of the coating decrease. Nevertheless, all Y_2O_3-modified coatings surpass the undoped Fe45 coating in both hardness and wear resistance. Appropriate Y_2O_3 doping effectively refines the Fe45 alloy coating's microstructure and induces lattice distortion, thereby enhancing its hardness and wear resistance.

Keywords: Fe-based alloy; laser cladding; rare-earth oxide; microstructure; tribological properties

CLC numbers: TG142 **Document code:** A **Article ID:** 1672-6421(2026)02-254-09

1 Introduction

Mechanical transmission components are usually fabricated from carbon steels due to their favorable machinability. However, the inherent limitations of carbon steel in hardness and wear resistance often lead to premature failure from excessive wear[1], significantly compromising service life. To mitigate this issue, metallic wear-resistant coatings are commonly applied to enhance surface durability. Among the various surface modification techniques available, laser cladding technology has gained increasing prominence for engineering applications on carbon steel components. This preference stems from its distinct advantages, including the production of coatings with finer microstructures, exceptionally narrow heat-affected zones (HAZ), and strong metallurgical bonding to the substrate. These characteristics generally superior to those achievable by conventional methods such as overlay welding[2], thermal spraying[3], and plasma cladding[4]. Thus, it is increasingly widely used in the engineering field.

Fe-based alloy coatings have been extensively utilized in aerospace, automotive manufacturing, and marine engineering due to their excellent mechanical properties and wear resistance, coupled with lower production costs compared to cobalt- and nickel-based counterparts. Compared to traditional carburizing and nitriding heat treatments for enhancing the wear resistance of carbon steel, the preparation of Fe-based alloy coatings via laser cladding offers simpler processing, higher efficiency, and superior control over coating thickness and hardness. The metallurgical

***Ming-xue Shen**

Male, Ph. D., Professor, Doctoral Supervisor. He is mainly engaged in the research of surface and interface performance regulation and life extension technology of key components of advanced equipment.

E-mail: shenmingxue@126.com

Received: 2025-03-19; Revised: 2025-06-16; Accepted: 2025-12-01

bond formed between the coating and the substrate results in a fusion zone, thus eliminating the risk of spalling caused by abrupt hardness transitions at interfaces between carburized/nitrided layers and the substrate[5-6]. Furthermore, laser cladding technology provides a cost-effective solution for localized repair of worn carbon steel components, making it particularly suitable for on-site remanufacturing of damaged parts. Nevertheless, laser cladding Fe-based coatings usually exhibit microstructural heterogeneities, including mixed morphologies of columnar crystals, dendrites, cellular crystals, and equiaxed grains, often accompanied by microvoids or cracks that significantly degrade coating performance[7-8]. Although process parameter optimization (e.g., laser power, scanning speed, scanning spacing), substrate preheating, and energy field assistance have been proposed to mitigate these defects[9-12], these approaches demonstrate limited effectiveness in microstructure homogenization while being time-consuming, technically challenging, and cost-ineffective.

Recent studies reveal that incorporating rare-earth oxides into alloy coatings can remarkably refine microstructures[13-14]. This enhancement mechanism involves the formation of heterogeneous nucleation sites with reduced surface energy through high-temperature interactions between rare earth elements and trace constituents (e.g., Si, C, O, Cr) in the alloy coating. The increased nucleation density during solidification promotes grain refinement. Furthermore, free rare-earth atoms can react with crack- and pore-sensitive elements such as S in the alloy coating, reducing the crack sensitivity and decreasing the pore defects in the coating, thereby improving the hardness and strength of the coating. Rare-earth oxides commonly used for doping and modifying alloy coatings include La_2O_3, CeO_2, Y_2O_3, etc.[14-17]. Notably, Y_2O_3 demonstrates superior microstructural refinement and mechanical enhancement at low doping concentrations due to the relatively large atomic radius and high electronegativity of the Y element[18-20]. Although rare-earth oxides evidently modify the microstructure and mechanical properties of laser cladding alloy coatings, their influence on tribological behavior, particularly for Y_2O_3-modified laser-clad Fe-based alloy coatings, remains poorly understood.

To bridge this knowledge gap and elucidate the wear mechanisms of Y_2O_3-doped Fe-based alloy coatings by laser cladding, the Y_2O_3-modified Fe45 alloy coatings on 20 steel substrates was fabricated via powder preplacement laser cladding process. The effects of Y_2O_3 content on microstructural evolution, hardness, and tribological behavior of the laser-clad Fe-based alloy coatings were systematically investigated. These findings will provide theoretical foundations and technical insights for engineering applications of rare-earth oxides in enhancing the mechanical and wear-resistant properties of Fe-based alloy coatings.

2 Experimental materials and methods

2.1 Materials

The substrate material for cladding was 20 steel (94 mm×45 mm×30 mm), with surfaces ground using abrasive paper to remove oxides and contaminants, followed by ultrasonic cleaning in anhydrous ethanol. The cladding system employed Fe45 alloy powder (15–53 μm particle size, chemical composition detailed in Table 1) blended with Y_2O_3 powder (1 μm average particle size). The Fe45 powder shown in Fig. 1 exhibits near-spherical morphology with smooth surfaces, ensuring excellent flow characteristics essential for the powder preset laser cladding process.

Table 1: Chemical composition of Fe45 alloy powder (wt.%)

C	B	Si	Cr	Ni	Fe
1.0	4.2	4.6	16.8	12.4	Bal.

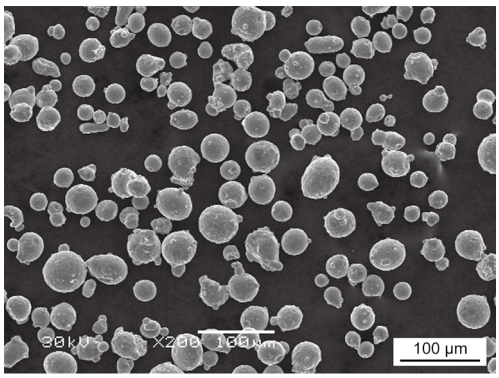

Fig. 1: SEM morphology of Fe45 alloy powder

2.2 Coating fabrication

The preparation process of the Y_2O_3-modified laser-clad Fe-based alloy coating is shown in Fig. 2. A vacuum mixer was used to prepare four Fe45 alloy powder mixtures with Y_2O_3 contents of 0wt.%, 0.3wt.%, 0.6wt.%, and 0.9wt.%, respectively. The rotation speed of the mixer was 120 $r \cdot min^{-1}$, and the mixing time was 5 h. The mixed powder was placed in a vacuum drying oven for drying treatment at a temperature of 100 °C for 2 h. The 20 steel substrate was installed on the build platform of the EP-M150 Metal 3D Printer, and the mixed powder was loaded into the powder bin of the equipment. Optimized process parameters, determined through

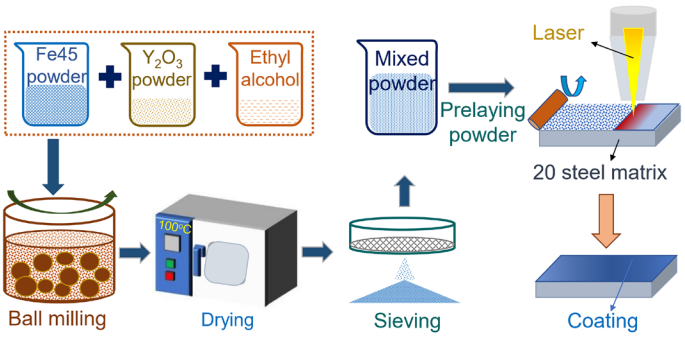

Fig. 2: Schematic diagram of laser cladding process

preliminary experiments, were employed: a laser power of 120 W, scanning speed of 400 mm·s^{-1}, scanning spacing of 0.07 mm, layer thickness of 0.05 mm, and a substrate preheating temperature of 100 °C. High-purity argon was used as the protective gas to avoid oxidation during the cladding process. After the coating was prepared, the specimens of the required size were obtained by wire-cutting process.

2.3 Characterization techniques

The metallographic structure of laser-clad Fe45 alloy coating was observed using an OLYMPUS BX53 M industrial microscope. The phase constitution of the laser-clad Fe-based alloy coating was analyzed using an XRD-6100 X-ray diffractometer. The structure morphology and the worn surface morphology of the coating were characterized by a Phenom XL G2 field emission scanning electron microscope. The elemental analysis of the worn surface was performed using an energy dispersive spectrometer (EDS). The three-dimensional morphology of the worn surface of the Fe-based alloy coating was analyzed using an optical profiler ZeGage^{TM} Pro. A Swiss HV5-50 Vickers hardness tester was used to test the hardness of the coating surface and cross-section, as well as the change in micro-hardness from the coating surface to the substrate. The schematic diagram of the micro-hardness testing method for the coating cross-section is shown in Fig. 3. The Vickers hardness of the coating was tested in the vertical direction from the top of the coating to the substrate at intervals of 0.2 mm in turn. The load was 3 N, and the holding time was 10 s.

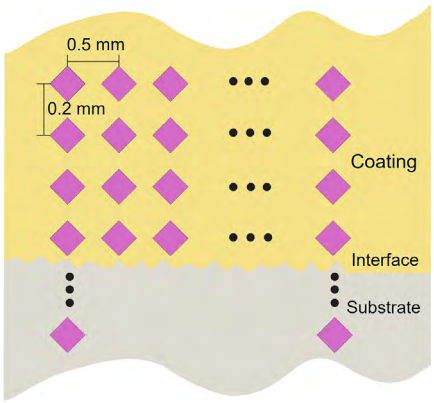

Fig. 3: Schematic diagram of micro-hardness testing method for coating cross-section

2.4 Tribological testing

The coating specimens were subjected to a friction and wear test at room temperature on a multi-functional reciprocating friction tester. The schematic diagram of the friction tester is shown in Fig. 4. The specimen was fixed on the surface of the reciprocating platform, and the platform was driven to reciprocate by the rotation of the eccentric shaft driven by the motor. A GCr15 steel ball with a diameter of 8 mm was selected as the counter-friction pair. The steel ball was fixed in the hollow cylindrical arm directly above the reciprocating platform, and an external force was loaded onto the friction interface through the hollow cylindrical arm. The hollow cylindrical arm was connected to the normal force sensor and the radial force sensor to realize real-time monitoring of the normal stress and shear stress of the steel ball during the friction process. The external load used in the friction test was 15 N, the friction frequency was 4 Hz, the reciprocating distance was 5 mm, and the time was 30 min.

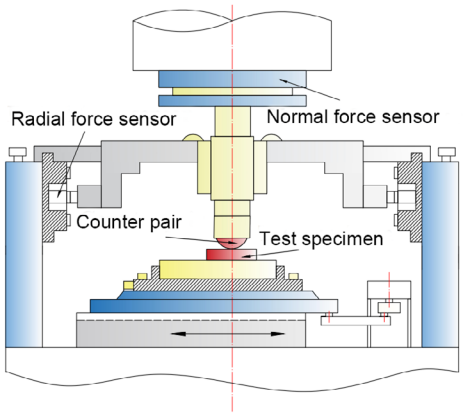

Fig. 4: Schematic diagram of multi-functional reciprocating friction tester

3 Results and discussion

3.1 Microstructure of Y_2O_3-doped laser-clad Fe45 alloy coatings

The cross-sectional metallographic microstructures of laser-clad Fe45 alloy coatings with different Y_2O_3 contents are shown in Fig. 5. All coatings exhibit dense surfaces free from apparent crack defects. Figure 5(a) displays the microstructure of the undoped Fe45 alloy coating, where distinct molten pool boundaries are observed in localized regions, while other areas show diminished boundaries due to epitaxial growth of columnar crystals. Figure 5(b) shows the metallographic structure of the Fe45 alloy coating with 0.3wt.% Y_2O_3 addition, both the molten pool boundaries and the columnar crystal structure disappear entirely. When the Y_2O_3 content increases to 0.6wt.% [Fig. 5(c)], localized microstructure morphology becomes coarser. Further increasing Y_2O_3 to 0.9wt.% [Fig. 5(d)] results in alternating distributions of coarse and fine grains, with more severe coarsening compared to the 0.6wt.% sample. This fully indicates that appropriate rare earth oxide addition refines the microstructure of laser-clad Fe45 alloy coatings, whereas excessive doping deteriorates microstructural homogeneity.

Since rare earth doping modifies the metallographic structure of Fe45 alloy coatings, the phase constitution of the coating may also change. Figure 6 presents the XRD patterns of Fe45 alloy coatings with different Y_2O_3 contents. As can be seen from Fig. 6, the XRD pattern of the undoped Fe45 alloy coating mainly exhibits 6 diffraction peaks, which are $Fe_{0.7}Cr_{0.19}Ni_{0.11}$ (111) at 2θ=43.55°, α-Fe (110) at 2θ=44.45°, γ-(Fe, Ni) (200) at 2θ=50.6°, α-(Fe, Ni) (200) at 2θ=64.5°, γ-(Fe, Ni) (220) at 2θ=74.6°, and α-(Fe, Ni) (211) at 2θ=82°. The incorporation of Y_2O_3 preserves the number of diffraction

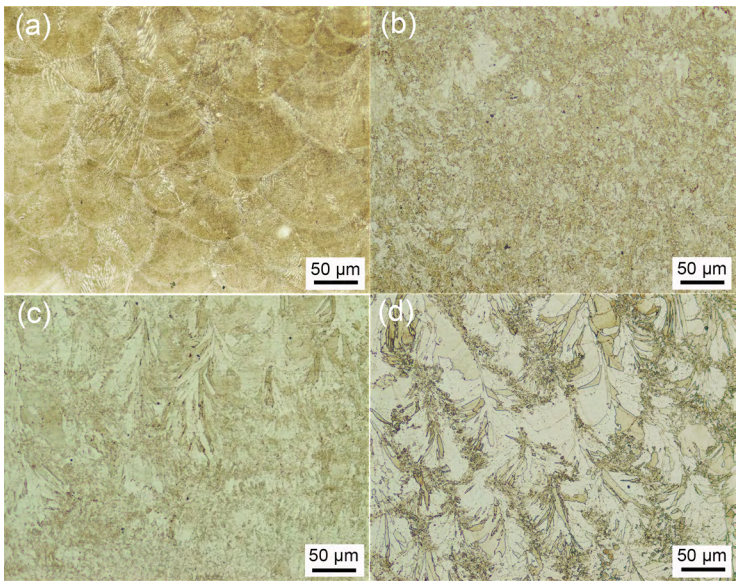

Fig. 5: Metallographic structure of laser-clad Fe45 alloy coatings with different Y_2O_3 contents: (a) 0wt.%; (b) 0.3wt.%; (c) 0.6wt.%; (d) 0.9wt.%

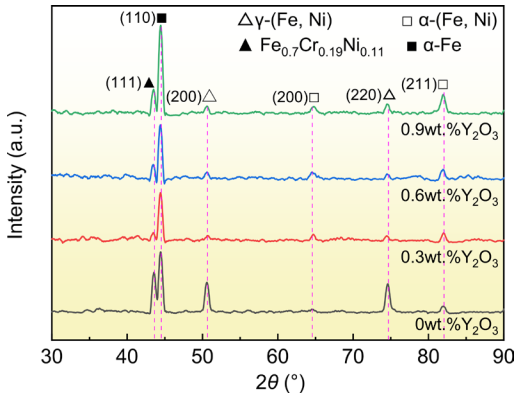

Fig. 6: XRD patterns of laser-clad Fe45 alloy coatings with different Y_2O_3 contents

peaks but induces angular shifts and intensity variations. After adding Y_2O_3, the diffraction peaks at 2θ=43.55°, 44.45°, 74.6°, and 82° shift to smaller angles, while the diffraction peak at 2θ=64.5° shifts to a larger angle. In addition, no peaks corresponding to Y_2O_3 phase or any new Y-containing phase are observed in the XRD diffraction pattern after adding Y_2O_3, likely due to the Y_2O_3 concentration falling below the XRD detection threshold.

To further analyze the evolution behavior of the microstructure of the Fe45 alloy coating doped with Y_2O_3, the cross-sectional microstructures of Fe45 alloy coatings with different Y_2O_3 contents were observed by SEM, and their morphological characteristics are shown in Fig. 7. Figures 7(a1–d1) are the enlarged views of the white box areas in Figs. 7(a–d) respectively, and the EDS patterns are obtained by area scanning in Figs. 7(a1–d1). As can be seen from Fig. 7(a), there are many columnar crystals in the microstructure of the undoped Fe45 alloy coating. Through the local enlarged view [Fig. 7(a1)], it can be seen that there are also cellular crystals in the metallographic structure. The distribution of the main elements in the Fe45 alloy is relatively uniform, with no obvious element segregation observed.

When 0.3wt.% Y_2O_3 is added, as shown in Fig. 7(b), the size and quantity of columnar crystals in the coating are significantly decreased, and the microstructure is replaced by fine cellular and equiaxed grains [Fig. 7(b1)]. The Y element is distributed relatively uniformly throughout the coating and does not disrupt the uniform distribution of the elements in the Fe45 alloy. This refinement originates from Y^{3+} ions released during laser cladding, which enhance molten pool nucleation rates and suppress columnar crystal growth[21]. The 0.6wt.% Y_2O_3 doped Fe45 alloy coating develops localized "feather-like" coarsened structures [Fig. 7(c)], which is similar to the microstructure observed in Fig. 5(c). By magnifying the "feather-like" coarsened structure, it is found that the structure is composed of fine equiaxed crystals. The microstructure morphology of other areas is similar to that of the 0.3wt.% Y_2O_3 doped Fe45 alloy coating. Both Y and base alloy elements remain uniformly distributed. At 0.9wt.% Y_2O_3 content, as shown in Fig. 7(d), "feather-like" structures dominate, again similar to the metallographic observations. Through the enlarged view of the "feather-like" coarsened structure, it is also found that the structure is composed of fine equiaxed crystals.

The distributions of the Y element and the main elements of the Fe45 alloy are both relatively uniform, which indicates that the "feather-like" coarsened structure is not caused by the segregation of rare-earth elements. This change may be due to the increase of Y_2O_3 addition, which enhances the laser absorption rate of Fe45 alloy powder, thereby raising the temperature of the molten pool. The resulting reduction in cooling rate and time prolong the grain growth period[22]. At the same time, the excess of rare-earth elements will intensify the solute redistribution effect, significantly expanding the constitutional supercooling zone. The dendrites grow in a non-equilibrium state, and branches form around the main trunk, presenting a "feather-like" morphology. In addition, since the rare-earth oxide acts as a heterogeneous nucleation

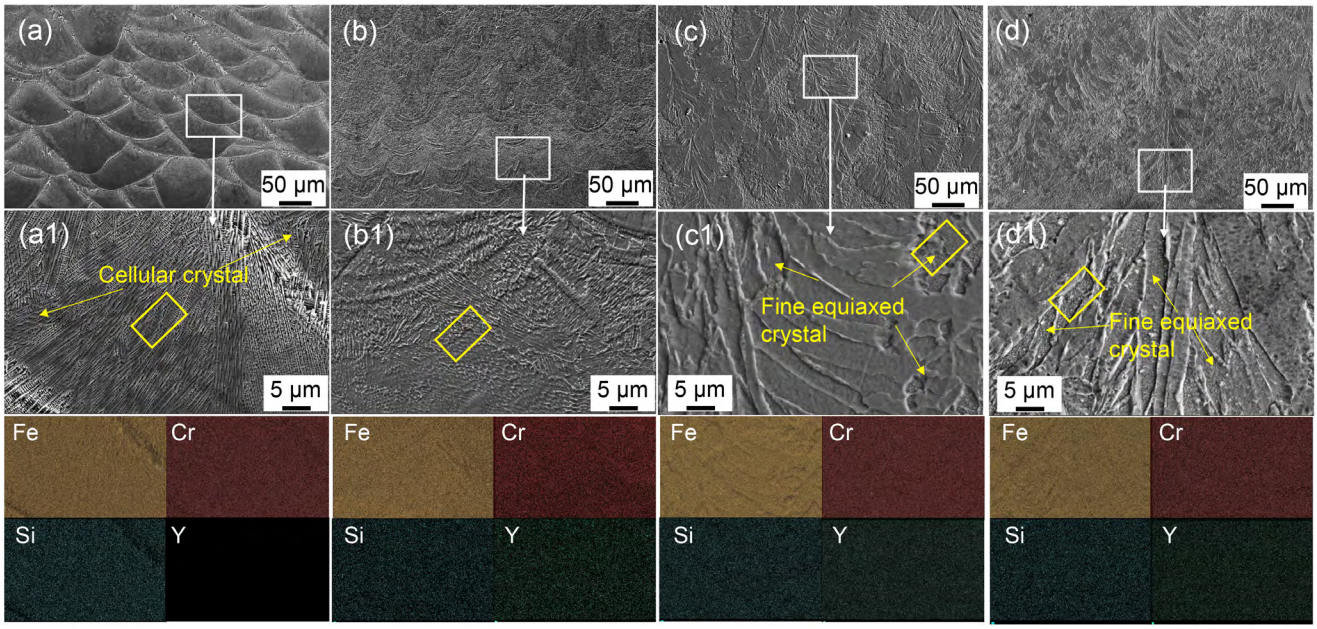

Fig. 7: SEM and EDS images of laser-clad Fe45 alloy coatings with different Y_2O_3 contents: (a) 0wt.%; (b) 0.3wt.%; (c) 0.6wt.%; (d) 0.9wt.%

site within the molten pool and expands the constitutional supercooling zone, the nucleation rate is significantly increased. The equiaxed crystals grow to fill the interdendritic gaps, thus forming a "feather-like" coarsened structure with dendrites serve as the skeleton and equiaxed crystals filling the gaps between them.

The grain size within the yellow boxed areas in Figs. 7(a1–d1) was analyzed using ImageJ statistical software, the results are shown in Fig. 8. It can be seen that a decreasing trend in grain size with increasing Y_2O_3 content. This grain refinement effect may positively influence the hardness and wear resistance of the Fe45 alloy coating. Typically, grain refinement increases the grain boundary area, making it more difficult for dislocations to traverse the grain boundaries, which enhances the material's hardness and wear resistance.

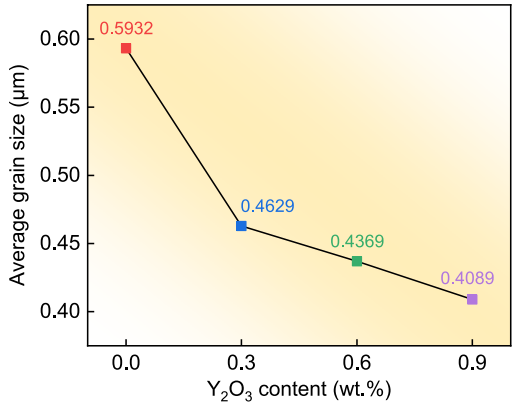

Fig. 8: Average grain size of laser-clad Fe45 alloy coatings with different Y_2O_3 contents

3.2 Microhardness of Y_2O_3-doped laser-clad Fe45 alloy coatings

Figure 9 shows the surface microhardness of laser-clad Fe45 alloy coatings with different Y_2O_3 contents. As can be seen

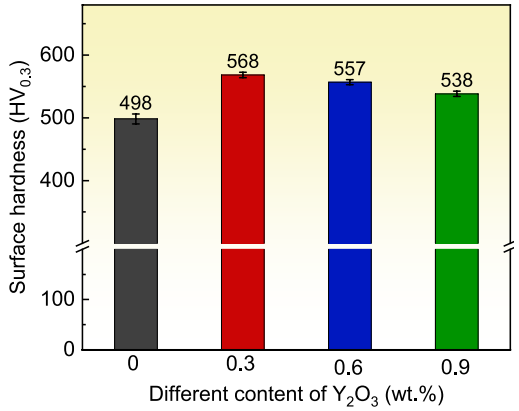

Fig. 9: Surface microhardness of laser-clad Fe45 alloy coatings with different Y_2O_3 contents

from Fig. 9, the surface microhardness of the Fe45 alloy coatings with Y_2O_3 addition is higher than that of undoped Fe45 alloy coating. When Y_2O_3 is not added, the surface microhardness of the Fe45 alloy coating is 498±8 $HV_{0.3}$. As the Y_2O_3 content gradually increases to 0.9wt.%, the surface microhardness of the Fe45 alloy coating firstly increases and then gradually decreases. When the Y_2O_3 amount is 0.3wt.%, the surface microhardness of the Fe45 alloy coating is the highest, which is 568±4 $HV_{0.3}$, an increase of 14.06% compared with the surface microhardness of the undoped Fe45 alloy coating.

The cross-section microhardness of Fe45 alloy coatings with different Y_2O_3 contents is shown in Fig. 10. The abscissa in Fig. 10 represents the distance from the indentation position of the Vickers hardness tester to the coating surface. It can be seen from Fig. 10 that the cross section of Fe45 alloy samples with different Y_2O_3 contents consists of three regions, namely coating region, heat affected zone, and substrate region. The cross-section microhardness of the Fe45 alloy coating without Y_2O_3 shows little fluctuate, and its value is maintained at about

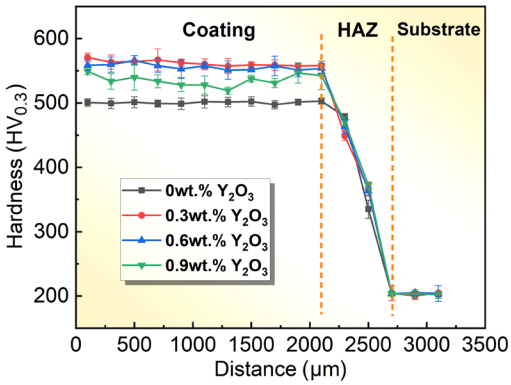

Fig. 10: Cross-sectional microhardness of laser-clad Fe45 alloy coatings with different Y_2O_3 contents

500 $HV_{0.3}$, which is equivalent to the hardness value of the coating surface shown in Fig. 9. The hardness value of the heat affected zone gradually decreases with the increase of the distance from the surface. The hardness value of the substrate 20 steel is about 200 $HV_{0.3}$, which is much lower than that of the coating. After adding different contents of Y_2O_3, the change trend of the hardness of the three regions in the specimen cross-section with the distance is similar to that of the specimen without Y_2O_3. When the Y_2O_3 content is 0.3wt.%, the cross-sectional hardness of the coating increases significantly, averaged at 562 $HV_{0.3}$. When the Y_2O_3 content increases to 0.6wt.% and 0.9wt.%, the average cross-sectional hardness of the coating is 556 $HV_{0.3}$ and 535 $HV_{0.3}$, respectively, showing a downward trend compared to 0.3wt.% Y_2O_3. The cross-sectional hardness of the coating exhibits more obvious fluctuation; however, all hardness values remain higher than that of the coating without Y_2O_3.

Based the surface and cross-sectional hardness measurements of Fe45 alloy coatings with different Y_2O_3 contents, it can be seen that the appropriate addition of Y_2O_3 can significantly improve the microhardness of the Fe45 alloy coating, while excessive Y_2O_3 lead to a reduction in microhardness. Combined with Fig. 6 and Fig. 7, it can be known that after the addition of Y_2O_3, the columnar crystals in the Fe45 alloy coating transform into finer equiaxed crystals, and the lattice is distorted, which will inevitably increase the coating hardness. However, after excessive rare-earth addition, the "feather-like" coarsened structure in the coating gradually increases, which increases the grain size of the coating structure, resulting in a decrease in the coating hardness.

3.3 Tribological behavior of Y_2O_3-doped laser-clad Fe45 alloy coatings

The friction and wear behavior of Fe45 alloy coatings with different Y_2O_3 contents were evaluated at room temperature using a multifunctional reciprocating friction tester. The resulting friction coefficient curves and their average values are presented in Fig. 11. The change trends of all curves are very similar. The friction coefficient increases sharply at the initial stage of running-in, and then decreases rapidly and finally tends to be stable. Both have experienced the running-in stage and the stable wear stage. This is mainly due to the fact that the asperities on the coating surface contact with the GCr15 ball at the initial running-in stage, and the friction resistance is large, so that the friction coefficient is significantly increased. The change in the rising rate of the friction coefficient of Fe45 alloy coatings with different Y_2O_3 contents is consistent with the change in the surface microhardness of Fe45 alloy coatings with different Y_2O_3 contents (as shown in Fig. 9), indicating that the higher the surface hardness of the coating, the more unstable the friction coefficient at the initial running-in stage, and the running-in period of the coating prolongs with the increase in the Y_2O_3 content. When the asperities are gradually crushed by repeated extrusion and shearing, the friction resistance decreases accordingly, manifested as a gradual decrease and stabilization of the friction coefficient. At the same time, some wear debris shed from the friction pair is not transferred out of the friction area in time and remains on the friction interface, resulting in fluctuations in the friction coefficient[23–25]. In the stable wear stage, as the Y_2O_3 content increases, the average friction coefficient of the Fe45 alloy coating shows a decreasing trend [(as shown in Fig. 11(b)]. When the Y_2O_3 content is 0.9wt.%, the average friction coefficient of the coating is about 0.4, which is 20% lower than that of the Fe45 alloy coating without Y_2O_3.

Figure 12 shows the three-dimensional morphology and two-dimensional cross-sectional profile of the worn surfaces of

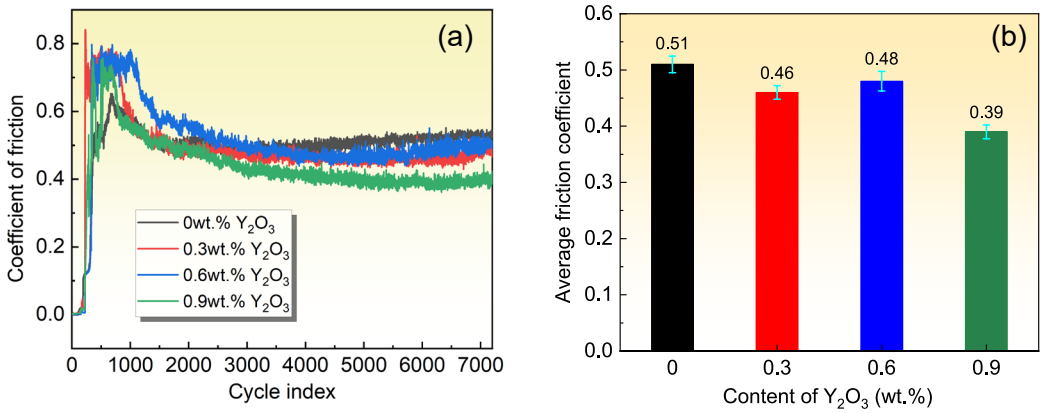

Fig. 11: Friction coefficient curves (a) and average friction coefficient (b) of laser-clad Fe45 alloy coatings with different Y_2O_3 contents

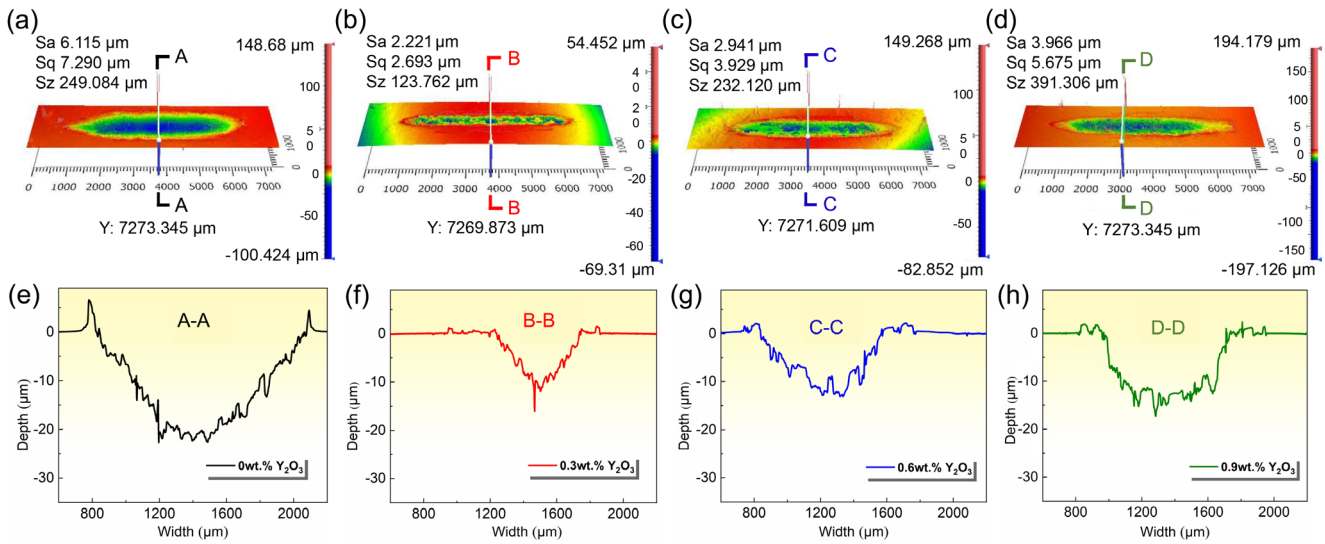

Fig. 12: Three-dimensional morphology and two-dimensional cross-sectional profile of worn surfaces of laser-clad Fe45 alloy coatings with different Y_2O_3 contents: (a, e) 0wt.%; (b, f) 0.3wt.%; (c, g) 0.6wt.%; (d, h) 0.9wt.%

Fe45 alloy coatings with different Y_2O_3 contents. It can be seen from the three-dimensional profile of the worn coating surface [Figs. 12(a–d)], as the Y_2O_3 content increases from 0wt.% to 0.9wt.%, the surface roughness of the worn coating firstly decreases and then increases. The surface roughness of all the worn coatings with Y_2O_3 addition is significantly smaller than that of the worn coating without Y_2O_3 addition. When the Y_2O_3 content is 0.3wt.%, the minimum surface roughness of the worn coating is obtained. In addition, as shown in the two-dimensional cross-sectional profile of the coating wear track [Figs. 12(e–f)], the width and depth of the wear track firstly decrease and then increase with an increase in Y_2O_3. The width and depth of the wear track on the coating without Y_2O_3 addition are the largest, while those on the coating with 0.3wt.% Y_2O_3 addition are the smallest, with a width of about 500 μm and a depth of about 12 μm. In summary, the morphology analysis of the worn surfaces reveals that the addition of Y_2O_3 significantly enhances the wear resistance of the Fe45 alloy coatings. This improvement is content-dependent and exhibits an optimal value at 0.3wt.%. At this specific content, the surface roughness, wear track width and depth are all minimized, demonstrating the best anti-wear performance. These findings indicate that an appropriate amount of Y_2O_3 effectively enhances the stability of the coating material during the wear process, while excessive addition may conversely lead to detrimental effects.

The wear volumes of Fe45 alloy coatings with different Y_2O_3 contents were approximated using two-dimensional cross-sectional profiles of wear tracks [Figs. 12(e–f)], with results summarized in Fig. 13. The undoped coating exhibits a wear volume of 3,553.12 μm^3. Upon addition of 0.3wt.% Y_2O_3 the wear volume sharply decreases to 1,735.41 μm^3, representing a 51.16% reduction. As the Y_2O_3 content gradually increases to 0.9wt.%, the wear volume shows a gradual upward trend, but it is much lower than that of the coating without the addition of Y_2O_3. This pattern confirms that Y_2O_3 doping significantly enhances the wear resistance of

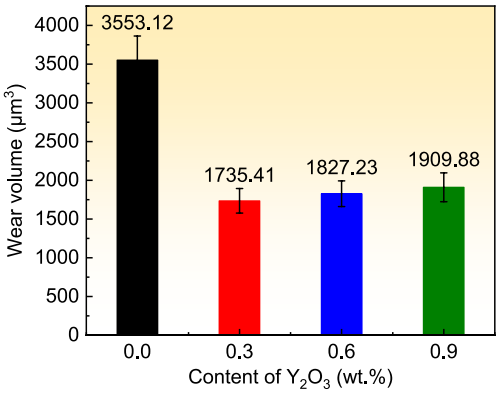

Fig. 13: Wear amounts of laser-clad Fe45 alloy coatings with different Y_2O_3 contents

Fe45 alloy coatings.

During the friction process, the penetration depth of counterface asperities into the coating is closely related to the coating's hardness. Combined analysis of surface and cross-sectional hardness data (Fig. 9 and Fig. 10) reveals that Y_2O_3 doping increases the hardness of Fe45 alloy coatings. Higher coating hardness reduces both the indentation depth of counterpart asperities and the resultant wear track dimensions. Consequently, the 0.3wt.% Y_2O_3-doped coating, which demonstrates peak hardness values, achieves minimal wear track width and depth, naturally leading to the smallest wear volume.

To elucidate the wear mechanisms of Y_2O_3-doped laser-clad Fe45 alloy coatings, SEM and EDS analyses were conducted on wear morphologies, with results presented in Fig. 14. Figures 14(a1–d1) are the enlarged views of the yellow boxed areas in Figs. 14(a–d) correspondingly, and the element distribution maps are obtained by EDS area scanning in Figs. 14(a1–d1). The area between the two red dotted lines in Figs. 14(a–d) is the wear area. The undoped Fe45 alloy coating [Fig. 14(a)] displays a wide wear track with no prominent grooves, but shows minor scratches and an obvious plastic deformation layer. Bright white particles are observed on the deformation layer surface, attributed to the substantial

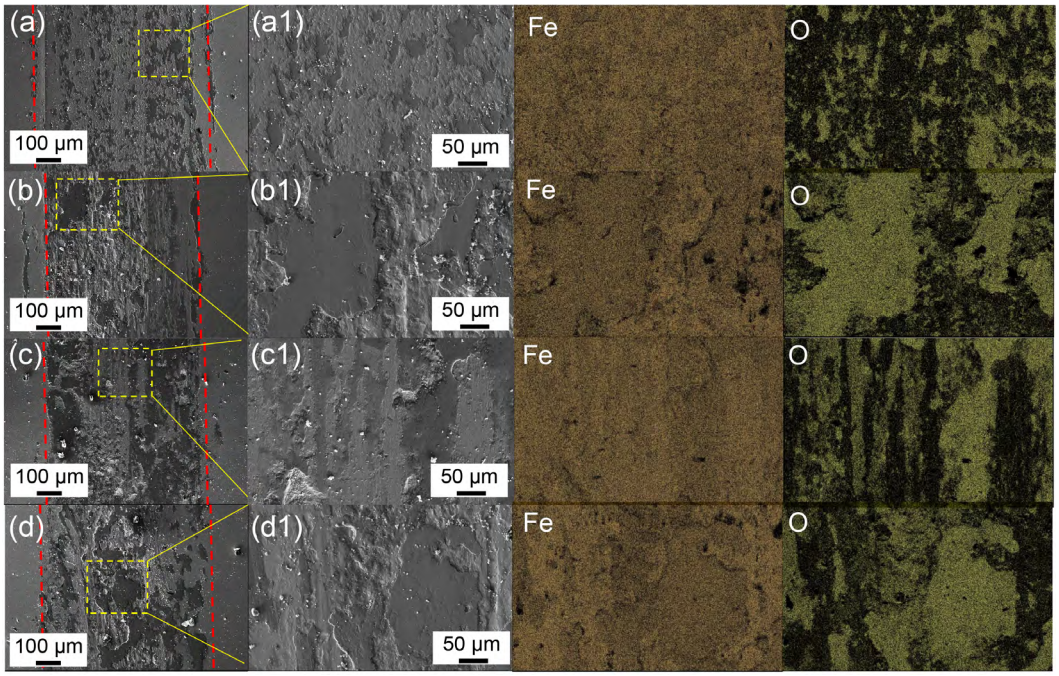

Fig. 14: Abrasion morphology and EDS images of laser-clad Fe45 alloy coatings with different Y_2O_3 contents: (a) 0wt.%; (b) 0.3wt.%%; (c) 0.6wt.%; (d) 0.9wt.%

hardness difference between the GCr15 counterpart ball and the Fe45 coating. During the friction process, elevated surface temperatures facilitate the embedding of wear debris into the coating by the harder counterpart, and scrape the wear surface to form scratches. The coating is also subjected to complex alternating stress loads, resulting in serious adhesive wear and fatigue wear of the coating. EDS analysis reveals extensive oxygen-enriched zones on the wear surface, confirming concurrent oxidative wear behavior in undoped Fe45 alloy coating. When the addition of Y_2O_3 is 0.3wt.%, the wear track width is significantly reduced, and the plastic deformation layer on the wear surface is also significantly reduced. However, the deformation layer surface becomes rougher. This phenomenon results from lattice distortion-induced internal stresses generated by Y_2O_3 doping during laser cladding, which simultaneously enhances coating hardness and suppresses crack initiation and propagation during the friction process, thereby improving resistance to adhesive and fatigue wear of the Fe45 alloy coating[25].

When the addition of Y_2O_3 increases from 0.6wt.% to 0.9wt.%, the wear track width slightly increases, and the surface of the plastic deformation layer gradually becomes smooth. This deterioration correlates with reduced coating hardness at higher Y_2O_3 concentrations, which exacerbates adhesive and fatigue wear mechanisms. From the EDS results in Fig. 14, substantial oxygen accumulation is observed on the worn surfaces of the Y_2O_3-doped Fe45 alloy coatings, further confirming the occurence of oxidative wear behavior. Combined with the elemental data from the wear surfaces (Fig. 15), the observed decrease in oxygen content with higher Y_2O_3 concentrations shows that such doping inhibits oxidative wear. Consequently, the oxidation-wear resistance of the Fe45 alloy coating improves linearly with the Y_2O_3 doping amount.

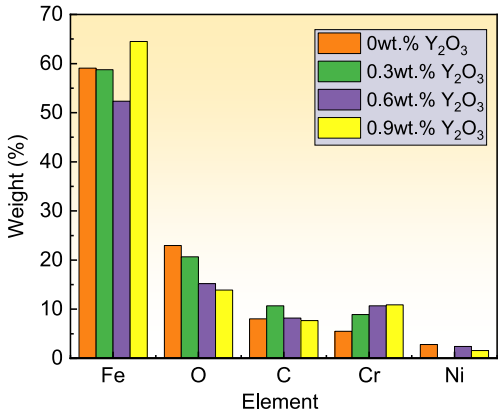

Fig. 15: Elemental content in worn surface of laser-clad Fe45 alloy coatings with different Y_2O_3 contents: (a) 0wt.%; (b) 0.3wt.%; (c) 0.6wt.%; (d) 0.9wt.%

4 Conclusions

Laser cladding technology was employed to fabricate Y_2O_3-doped Fe45 alloy coatings on 20 steel substrates, and the effects of Y_2O_3 content on the microstructure, hardness, and tribological properties were systematically investigated. The key conclusions are summarized as follows:

(1) Y_2O_3 doping significantly alters the microstructure of laser-clad Fe45 alloy coatings. At 0.3wt.% Y_2O_3 addition, the coating exhibits optimal refinement, dominated by cellular and equiaxed crystals. As the Y_2O_3 content increases to 0.9wt.%, the microstructure transitions to a coarsened "feather-like" morphology, characterized by dendritic skeletons filled with equiaxed grains.

(2) The microhardness of the coating firstly increases and then decreases with increasing Y_2O_3 content, reaching a peak of 568±4 $HV_{0.3}$ at 0.3wt.%, which is a 14.06% enhancement over

the Y_2O_3-free coating (498±8 $HV_{0.3}$). This trend is governed by the Y_2O_3-induced microstructural homogeneity, grain refinement, and lattice distortion.

(3) The friction coefficient of the laser-clad Fe45 alloy coatings progressively decreases with increasing Y_2O_3 doping, while the wear volume firstly reduces and then increases. The 0.3wt.% Y_2O_3-doped Fe45 alloy coating demonstrates optimal wear resistance, achieving a 51.16% reduction in wear volume compared to the undoped Fe45 alloy coating.

(4) Undoped Fe45 coatings primarily suffer from adhesive wear and fatigue wear, accompanied by oxidative wear and slight abrasive wear. Y_2O_3 doping enhances both hardness and oxidation resistance, leading to substantial mitigation of adhesive and fatigue wear.

Acknowledgments

This work was supported by the Jiangxi Provincial Natural Science Foundation of China (Grant number 20224BAB204049), the Fund Project of Jiangxi Provincial Department of Education (Grant number GJJ2200602), and the National Natural Science Foundation of China (Grant number 52205194).

Conflict of interest

The authors declare that they have no known competing financial interests or personal relationships that could have appeared to influence the work reported in this paper.

References

[1] Casey S B, John H, Matthew E, et al. Niobium-darbide-enhanced wear performance of high-carbon steels. Steel Research International, 2024, 95(3): 1–6.
[2] Yu Q, Zhang W, Shang J, et al. Comparative investigation on the microstructure and corrosion properties of surfacing cobalt alloys by various methods. Surface & Coatings Technology, 2024, 494: 131386.
[3] Zhao X Y, Li C, Li S Y, et al. Mechanism study on the influence of combustion models and spray gun geometric parameters on high-velocity oxygen-fuel (HVOF) thermal spraying. Journal of Manufacturing Processes, 2023, 98: 173–185.
[4] Xie Y J, Wen X, Yan J K, et al. Microstructure and wear resistance of $AlCoCrFeNiCuSn_x$ high-entropy alloy coatings by plasma cladding. Vacuum, 2023, 214: 112176.
[5] Jurči P. History, developments and trends in the heat treatment of steel. Materials, 2020, 13(18): 4003.
[6] Dong Y, Cui X, Li J, et al. Effect of carburizing nitriding compound treatment on microstructure evolution and properties of low carbon gear steel. Materials Chemistry and Physics, 2025, 337: 130489.
[7] Li C, Sun R W, Li Y L, et al. Wear mechanism of a laser cladded Fe-based self-lubricating composite coating for protecting counter-abrasive parts. Surface and Coatings Technology, 2023, 459: 129402.
[8] Wang J Y, Cui X F, Jin G, et al. Effect of in-situ Ni interlayer on the microstructure and corrosion resistance of underwater wet 316L stainless steel laser cladding layer. Surface and Coatings Technology, 2023, 458: 129341.
[9] Karmakar D P, Muvvala G, Nath A K. Effect of scan strategy and heat input on the shear strength of laser cladded Stellite 21 layers on AISI H13 tool steel in as-deposited and heat treated conditions. Surface and Coatings Technology, 2020, 384: 125331.
[10] Zhu Z C, Li J F, Peng Y X, et al. In-situ synthesized novel eyeball-like Al_2O_3/TiC composite ceramics reinforced Fe-based alloy coating produced by laser cladding. Surface and Coatings Technology, 2020, 391: 125671.
[11] Zhang J, Zhao C J, Bai Q F, et al. Effect of ultrasonic high-frequency percussion on the microstructure and corrosion resistance of Fe-based alloy coatings by high-speed laser cladding. Materials Letters, 2023, 335: 133769.
[12] Hu Y, Wang L, Chen Z J, et al. Effects of electromagnetic compound field on the dendrite growth of laser cladding. Surface and Coatings Technology, 2023, 453: 129118.
[13] Wang Q, Yang J, Niu W J, et al. Effect of La_2O_3 on microstructure and properties of Fe-based alloy coatings by laser cladding. Optik, 2021, 245: 167653.
[14] Cai Y C, Luo Z, Chen Y, et al. Influence of CeO_2 on tribological behavior of TiC/Fe-based composite coating. Surface Engineering, 2017, 33(12): 1–8.
[15] Wang W J, Fu Z K, Cao X, et al. The role of lanthanum oxide on wear and contact fatigue damage resistance of laser cladding Fe-based alloy coating under oil lubrication condition. Tribology International, 2016, 94: 470–478.
[16] Zhao Y H, Jie S, Li J F. Effect of rare earth oxide on the properties of laser cladding layer and machining vibration suppressing in side milling. Applied Surface Science, 2014, 321(1): 387–395.
[17] Liu X Y, Sui Y, Li J B, et al. Laser metal deposited steel alloys with uniform microstructures and improved properties prepared by addition of small amounts of dispersed Y_2O_3 nanoparticles. Materials Science and Engineering: A, 2021, 806: 140827.
[18] Tian Y S, Chen C Z, Chen L X, et al. Effect of RE oxides on the microstructure of the coatings fabricated on titanium alloys by laser alloying technique. Scripta Materialia, 2006, 54(5): 847–852.
[19] Li H C, Wang D G, Chen C Z, et al. Effect of CeO_2 and Y_2O_3 on microstructure, bioactivity and degradatility of laser cladding CaO-SiO_2 coating on titanium alloy. Colloids and Surfaces, B: Biointerfaces, 2015, 127: 15–21.
[20] Wang K L, Zhang Q B, Sun M L, et al. Rare earth elements modification of laser-clad nickel-based alloy coatings. Applied Surface Science, 2001, 174: 191–200.
[21] Guo T, Pu Y, Zhang R, et al. Influence of Y_2O_3 content on microstructure and properties of laser cladding 0.3C-18Cr alloy coating. Rare Metal Materials and Engineering, 2019, 48(11): 3643–3650.
[22] Zhang Z, Yang F, Zhang H, et al. Influence of CeO_2 addition on forming quality and microstructure of TiC_x-reinforced $CrTi_4$-based laser cladding composite coating. Materials Characterization, 2021, 171: 110732.
[23] Sirikarn S, Visittapong Y, Tuksadon W, et al. Stress-induced, debris-modulated friction and wear resistance performance of nanostructured Ni-Co coatings. Wear, 2024, 538–539: 205184.
[24] Xiang Z, Liu G, Xie S, et al. The effect of interfacial wear debris on the friction-induced stick-slip vibration. Tribology International, 2024,199: 109999.
[25] Zhou H Y, Li L Y, Zhao Y, et al. Review of rate earth oxide doping-modified laser cladding of Fe-based alloy coatings. China Foundry, 2025, 22(1): 12–22.